# Assessments of Doppler Velocity Errors of EarthCARE Cloud Profiling Radar Using Global Cloud System Resolving Simulations: Effects of Doppler Broadening and Folding

Yuichiro Hagihara, Yuichi Ohno, Hiroaki Horie, *Member, IEEE*, Woosub Roh, Masaki Satoh, Takuji Kubota, *Member, IEEE*, and Riko Oki

***Abstract*— The Earth Clouds, Aerosol, and Radiation Explorer (EarthCARE) is a satellite mission jointly developed by the Japan Aerospace Exploration Agency (JAXA) and the European Space Agency (ESA). One challenging feature of this mission is the observation of Doppler velocity by the Cloud Profiling Radar (EC-CPR). The Doppler measurement accuracy is affected by random errors induced by Doppler broadening due to the finite beamwidth and Doppler folding caused by the finite pulse repetition frequency. We investigated the impact of horizontal (along-track) integration and unfolding methods on the reduction of Doppler errors, in order to improve Doppler data processing in the JAXA standard algorithm. We simulated EC-CPR-observed Doppler velocities from pulse-pair covariances with the latest EC-CPR specifications using the radar reflectivity factor and Doppler velocity fields simulated by a satellite data simulator and a global cloud system resolving simulation. Two representative cases of a cirrus cloud and precipitation were examined. In the cirrus cloud case, the standard deviation of random error was decreased to 0.5 m/s for −10 dB $Z_e$ after 10-km horizontal integration. In the precipitation case, large falling speeds of precipitation caused Doppler folding errors due to larger Doppler velocities than that in the cirrus cloud case. When $Z_e$ is larger than −15 dB $Z_e$, the standard deviations of random error were less than 1.0 m/s after 10-km horizontal integration and unfolding.**

***Index Terms*— Doppler measurement accuracy, Earth Clouds Aerosol and Radiation Explorer (EarthCARE), Global Cloud System Resolving Models (GCSRMs), horizontal integration, spaceborne Doppler radar, unfolding method.**

## I. Introduction

THE Earth Clouds, Aerosol, and Radiation Explorer (EarthCARE; hereafter EC) is a satellite mission jointly developed by the Japan Aerospace Exploration Agency (JAXA) and the European Space Agency (ESA). Two active and two passive sensors will be installed on the EC satellite: Cloud Profiling Radar (CPR), ATmospheric LIDar (ATLID), Multi Spectral Imager (MSI), and Broadband Radiometer (BBR) [1]. The EC uses these sensors to provide global observations of the vertical profiles of clouds, aerosols, and precipitation, as well as the Earth's radiative budget thereby continuing measurements of CloudSat [2] and Cloud-Aerosol Lidar and Infrared Pathfinder Satellite Observation (CALIPSO) [3] in the A-Train constellation of satellites, which have led to revolutionary changes in our perspectives on Earth's climate [4].

The EC-CPR is the first spaceborne CPR with Doppler capability. Its frequency is 94 GHz, with vertical and horizontal range sampling of 100 and 500 m, respectively. The minimum detectable reflectivity is −36 dB$Z_e$ at the top of the atmosphere and is better than CloudSat CPR sensitivity (−28 dB$Z_e$) due to EC's lower orbit (∼400 km) and the EC-CPR's larger antenna (2.5 m). The EC-CPR is thus expected to detect thinner cirrus clouds and small water clouds in the lower atmosphere more frequently (e.g., [5]). Moreover, it can measure the vertical motion of clouds and precipitation globally. And such vertical motion has never been observed from space before. This capability is thus expected to improve the discrimination between clouds and precipitation from previous studies [6], [7], as well as the estimation of cloud microphysical parameters from the previous algorithms [8], [9]. Consequently, it will improve various parameterization schemes used in climate models for their future projections and deepen our understanding of aerosol, cloud, and precipitation processes [10]–[12].

Global Cloud System Resolving Models (GCSRMs) [13], [14] can simulate various cloud systems with finer resolution than a typical General Circulation Model (GCM). For example, these models can simulate the time evolution, structure, and life cycle of cloud systems without cumulus parameterization. These simulation results can be compared with satellite data without assuming subgrid clouds in a model's horizontal resolution.

A satellite data simulator is a forward model used to calculate signals like those of the CloudSat CPR, passive channels of microwave satellites, and infrared/visible channels of

Manuscript received May 26, 2020; revised October 26, 2020 and February 10, 2021; accepted February 16, 2021. Date of publication March 8, 2021; date of current version December 9, 2021. This work was supported by the National Institute of Information and Communications Technology; in part by JSPS KAKENHI under Grant JP20H01978; and in part by the Program for Promoting Technological Development of Transportation (Ministry of Land, Infrastructure, Transport and Tourism of Japan). *(Corresponding author: Yuichiro Hagihara.)*

Yuichiro Hagihara, Yuichi Ohno, and Hiroaki Horie are with the Applied Electromagnetic Research Institute, National Institute of Infomation and Communications Technology (NICT), Koganei 184-8795, Japan (e-mail: hagihara@nict.go.jp).

Woosub Roh and Masaki Satoh are with the Atmosphere and Ocean Research Institute, The University of Tokyo, Kashiwa 277-8564, Japan.

Takuji Kubota and Riko Oki are with the Earth Observation Research Center, Japan Aerospace Exploration Agency, Tsukuba 305-8505, Japan.

Digital Object Identifier 10.1109/TGRS.2021.3060828

geostationary satellites from the output of GCSRMs [15], [16]. Satellite data simulators have been used to evaluate and improve clouds and precipitation in GCSRMs, and also investigate the impact of data assimilation [15], [17]–[20]. There are several evaluation studies of a GCSRM using the CloudSat CPR [16], [21], [22]. Hashino *et al.* [16] demonstrated that a GCSRM reproduced observed characteristics in convective and stratiform clouds for a tropical cyclone and a mid-latitude frontal system by using the CloudSat CPR. Roh *et al.* [21] also evaluated microphysics schemes using cloud classifications based on the CloudSat CPR. In this study, we obtained simulated EC-CPR observation data with the same horizontal and vertical resolution as the EC-CPR using GCSRM output and a satellite data simulator.

There have also been several studies of Doppler velocity measurement from a high-speed spaceborne platform due to the measurement difficulties involved as compared with ground-based radar. For instance, Doppler spectrum width becomes broader due to the contamination of satellite motion, distributions of hydrometeor falling velocity, and turbulence within the beamwidth [23]. The maximum Doppler velocity ($V_{\max}$) determined by pulse repetition frequency (PRF, which is variable between 6100 and 7500 Hz) is 4.9 to 6.0 m/s for the EC-CPR. When the velocity exceeds $V_{\max}$, Doppler folding occurs. Then, the measured velocity is within the range of $-V_{\max} \sim +V_{\max}$.

The CPR beam pointing error resulting from attitude determination errors, thermal distortions of the antenna, and other factors cause Doppler errors [24]. In cases where the radar reflectivity factor of clouds or precipitation is horizontally inhomogeneous, the bias errors of velocity are discussed as being introduced by nonuniform beam filling (NUBF) [25], [26].

In this study, we focus on Doppler errors caused by Doppler broadening and folding, and also examine how to reduce such errors. The latest EC-CPR specifications, such as the latitude dependence of PRF and signal-to-noise ratio (SNR), are adopted to better understand the expected EC-CPR performance. The EC-CPR-observed Doppler velocities are calculated from pulse-pair covariances, which were simulated in this study using globally simulated EC-CPR data (i.e., radar reflectivity factor and Doppler velocity). Using those covariances, we investigate the effectiveness of horizontal (along-track) integration and the unfolding method, in order to evaluate and improve Doppler data processing in the JAXA standard algorithm.

Section II describes the EC-CPR simulation method, the horizontal integration method of measured Doppler velocity, and the unfolding method. Section III gives examples of the simulated Doppler velocities with those errors, as well as the application of our methods to the simulated velocities. Finally, Section IV summarizes our findings and future tasks.

## II. Data and Method

The global cloud and precipitation data were simulated by the Nonhydrostatic ICosahedral Atmospheric Model (NICAM) [27]–[29] as a GCSRM. The horizontal resolution is 3.5 km, and the vertical grid has 40 levels ([18]). The simulation started from 00:00Z on 15 June 2008, initialized with the $0.5° \times 0.5°$ European Center for Medium-range Weather Forecasting (ECMWF) Year of Tropical Convection analysis [30]. This study used the simulation data obtained at 00:00Z on 19 June 2008.

We obtained the observable data using a satellite data simulator, the Joint Simulator [16], [31]. We set up the same hydrometeor size distribution between the NICAM simulation and the Joint Simulator. The EC Active SEnsor simulator (EASE) [32]–[35] was used to simulate the radar reflectivity factor and Doppler velocity of the EC-CPR in the Joint Simulator. Note that the gas and particle attenuation is taken into account in the calculation of radar reflectivity factor, while Doppler velocity is the total velocity of hydrometer echo including reflectivity-weighted particle fall speed and vertical air motion. The orbit was simulated so that EC passes over the Equator at 14:00 local time in the descending node. Along the orbit of the satellite, by interpolating the EASE data to the EC-CPR resolution, we obtained curtain data of radar reflectivity factor ($Z_{\mathrm{e,jsim}}$) and Doppler velocity ($V_{\mathrm{jsim}}$) (hereinafter referred to as "NICAM/J-Sim data"). In the EC-CPR data processing, Doppler velocity is defined as radial Doppler velocity (i.e., downward motion is positive). Following this definition, we adopted the same sign of Doppler velocity.

We note that the highest horizontal resolution of the NICAM, the GCSRM used in this study, is 3.5 km, which is still coarser than the ~800 m footprint of EC-CPR. The NICAM/J-Sim data are used to improve not only the Doppler data processing but also other JAXA standard algorithms over the whole region. In the future, we plan to use higher-resolution of NICAM data when they become available.

We simulated the measured Doppler velocity ($V_{\mathrm{m}}$) as follows:

$$V_m = V_{\mathrm{jsim}} + V_{\mathrm{random}} \tag{1}$$

where $V_{\mathrm{random}}$ is the random error caused by the spread of Doppler velocities within the beamwidth. The probability density function of $V_{\mathrm{random}}$ is Gaussian with a mean of 0 and a variance, the square of the standard deviation of random error, $SD^2_{\mathrm{random}}$ as follows:

$$\mathrm{pdf}(x) = \frac{1}{\sqrt{2\pi} \cdot SD_{\mathrm{random}}} \exp\left\{-\frac{x^2}{2 \cdot SD_{\mathrm{random}}}\right\} \tag{2}$$

where $SD_{\mathrm{random}}$ is determined by perturbation approximation [36] as follows:

$$SD_{\mathrm{random}} = C\sqrt{\frac{\lambda^2}{32\pi^2 M \cdot \rho^2 \cdot \left(\frac{1}{\mathrm{PRF}}\right)^2}\left[\left(1+\frac{N}{S}\right)^2 - \rho^2\right]} \tag{3}$$

and $C$ is a correction factor. Note that we investigated the standard deviation of Doppler broadening calculated by the numerical simulation [37] and found that the values of perturbation approximation [36] multiplied by 1.3 agreed well with the numerical simulation. We thus set $C = 1.3$ in this study. The wavelength is $\lambda$ ($\lambda = 3.2$ mm for EC-CPR), $M$ is the number of pulse pairs within an integration length, $\rho$ is the correlation function, and $S/N$ is the SNR. In nominal

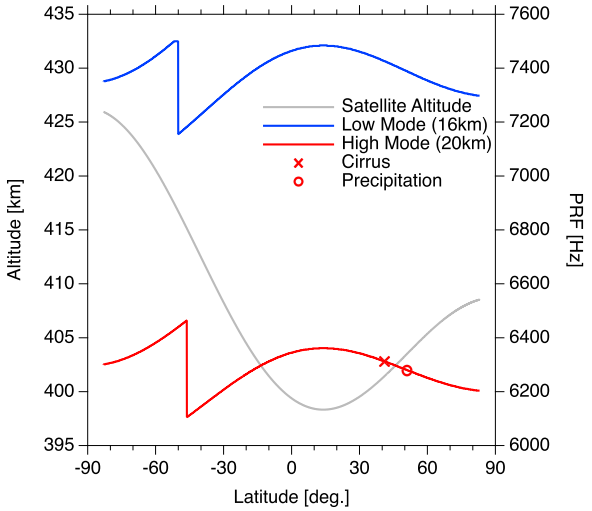


Fig. 1. Satellite altitude and PRF as a function of latitude and observation window mode. The symbols illustrate the cirrus (red cross) and precipitation (red circle) cases.

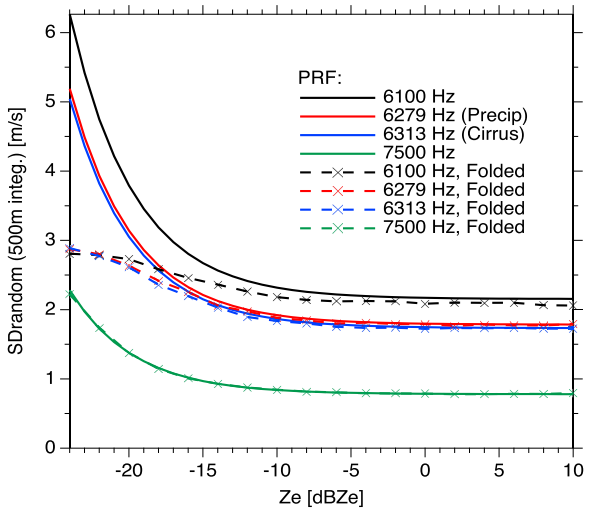


Fig. 2. Standard deviation of random error for 500-m integration as a function of $Z_e$ using the perturbation approximation method. The dashed lines denote random error considering Doppler folding.

operation, the EC-CPR will change the observation window, that is, low mode (−1 to 16 km) at latitudes of 60° to 90° and high mode (−1 to 20 km) at latitudes of 0° to 60°. The PRF changes in the range of 6100 to 7500 Hz with the latitude and observation window, as it is determined by the satellite altitude as illustrated in Fig. 1. This article focuses on the PRF of high mode. The number $M$ is 357 to 420 for 500-m integration depending on the PRF. The SNR is determined by the received echo power calculated from the radar equation and estimated EC-CPR noise level. In the case of EC-CPR, the SNR is 0 dB when a signal equivalent to −21.2 dB$Z_e$ is received. If $Z_{e,jsim}$ is less than −24 dB$Z_e$, we assume the Doppler velocity of its echo as being random noise in this study. The correlation function $\rho$ is defined as

$$\rho = \exp\left\{-8\left(\frac{\pi\cdot\sigma_v}{\lambda\cdot \mathrm{PRF}}\right)^2\right\} \tag{4}$$

where $\sigma_v$ is the total Doppler velocity spectrum width.

The spread $\sigma_v$ can be decomposed as follows:

$$\sigma_v^2 = \sigma_{\mathrm{psd}}^2 + \sigma_t^2 + \sigma_{\mathrm{sm}}^2 + \sigma_{\mathrm{ws}}^2 \tag{5}$$

where $\sigma_{\mathrm{psd}}$ is Doppler broadening due to the distributions of hydrometeor falling velocities and $\sigma_t$ is due to turbulence. We assumed $\sigma_{\mathrm{psd}} = 0.5$ m/s [38] and $\sigma_t = 1.0$ m/s [39]. $\sigma_{\mathrm{sm}}$ is the spread due to satellite motion, given by $\sigma_{\mathrm{sm}} \sim 0.3 V_{\mathrm{sat}}\theta_{3\,\mathrm{dB}}$, $V_{\mathrm{sat}}$ is the satellite velocity, and $\theta_{3\,\mathrm{dB}}$ is the beamwidth. When $V_{\mathrm{sat}}$ is 7738 m/s and $\theta_{3\,\mathrm{dB}}$ is 0.00166 rad (0.095°), $\sigma_{\mathrm{sm}}$ becomes 3.85 m/s. The broadening stems from wind shear and ranges from 0 to 1.0 m/s (e.g., [37], [40], [43]). However, it is not a significant contribution since the contribution of the satellite motion is as large as 3.85 m/s. In this study, we thus ignored the wind shear term ($\sigma_{\mathrm{ws}}$), so that $\sigma_v$ becomes 4.01 m/s.

Fig. 2 uses solid lines to plot $SD_{\mathrm{random}}$ for four PRFs in the case of 500-m integration. The range of PRFs for nominal EC-CPR operation is from 6100 to 7500 Hz. The PRFs of 6313 Hz and 6279 Hz correspond to the cirrus cloud and precipitation cases, respectively, as discussed in Section III. When $Z_e$ is less than −15 dB$Z_e$ (SNR = 6.2 dB), $SD_{\mathrm{random}}$ for each PRF increases significantly as $Z_e$ becomes smaller. When $Z_e$ is larger than −15 dB$Z_e$, however, small decreases are seen in $SD_{\mathrm{random}}$ for each PRF. The altitude dependence of SNR is negligible.

The EC-CPR measures Doppler velocities from the phase change of the echo between two successive pulses using the pulse-pair method. More than 350 real and imaginary parts of the pulse-pair are integrated onboard during a time corresponding to a 500 m along-track movement of the satellite. The integrated real and imaginary parts of pulse-pair covariances $R_\tau$ are simulated as follows:

$$\mathrm{Re}(R_\tau) = Z_{e,\mathrm{jsim}}\cdot\cos\left(\frac{4\pi\cdot V_m}{\lambda\cdot \mathrm{PRF}}\right) \tag{6}$$

$$\mathrm{Im}(R_\tau) = Z_{e,\mathrm{jsim}}\cdot\sin\left(\frac{4\pi\cdot V_m}{\lambda\cdot \mathrm{PRF}}\right). \tag{7}$$

Simulating the ground data processing, we define $V_{500\,\mathrm{m}}$ using 500-m integrated $R_\tau$ as follows:

$$V_{500\,\mathrm{m}} = \frac{\lambda\cdot\mathrm{PRF}}{4\pi}\tan^{-1}\left\{\frac{\mathrm{Im}(R_\tau)}{\mathrm{Re}(R_\tau)}\right\}. \tag{8}$$

In order to reduce random error, we conducted horizontal (along-track) integration, where 1- and 10-km horizontal integration of $R_\tau$ are calculated from 500-m integrated $R_\tau$ as follows:

$$V_{1\,\mathrm{km}} = \frac{\lambda\cdot\mathrm{PRF}}{4\pi}\tan^{-1}\left\{\frac{\sum_{1\,\mathrm{km}}\mathrm{Im}(R_\tau)}{\sum_{1\,\mathrm{km}}\mathrm{Re}(R_\tau)}\right\} \tag{9}$$

$$V_{10\,\mathrm{km}} = \frac{\lambda\cdot\mathrm{PRF}}{4\pi}\tan^{-1}\left\{\frac{\sum_{10\,\mathrm{km}}\mathrm{Im}(R_\tau)}{\sum_{10\,\mathrm{km}}\mathrm{Re}(R_\tau)}\right\} \tag{10}$$

where $V_{10\,\mathrm{km}}$ is produced for every km along the track distance using 20 successive $R_\tau$ as per (10), and the center location of 10-km integration is chosen to be the same as that of 1-km integration. As a suitable PRF is selected every second onboard (corresponding satellite movement length ∼ 7.7 km), the PRF does not change in 1-km integration length, so that $V_{1\,\mathrm{km}}$ can be calculated with simple integration as in (9). On the other hand, the PRFs are occasionally changed in 10-km

integration length. In this case, we separate the integration length into two periods, namely before and after the PRF changing point, and those Doppler velocities are calculated using each integrated $R_\tau$. The final $V_{10\,\mathrm{km}}$ is calculated from the pulse number-weighted average of both velocities.

An inherent characteristic of Doppler radar is Doppler velocity folding. $V_{\max}$ can be measured by the pulse-pair method and is defined by PRF ($V_{\max} = \lambda \cdot \mathrm{PRF}/4$). If $|V_{500\,\mathrm{m},\ 1\,\mathrm{km},10\,\mathrm{km}}|$ is larger than $V_{\max}$, Doppler folding affects $V_{500\,\mathrm{m},1\,\mathrm{km},10\,\mathrm{km}}$. For instance, with a PRF of 6100 Hz ($V_{\max} =$ 4.8 m/s), when the speed of the echo target is downward 6 m/s, it is measured as upward 3.6 m/s. The dashed lines in Fig. 2 denote $SD_{\mathrm{random}}$ as a function of $Z_{\mathrm{e}}$ for four PRFs considering this Doppler folding. These results are derived from the results of 10,000 simulations of $V_{500\,\mathrm{m}}$ using (8). In this simulation, $V_{\mathrm{jsim}} = 0$ is assumed. Comparing the solid lines of 6100, 6279, and 6313 Hz with the dashed lines of those PRFs, $SD_{\mathrm{random}}$ considering Doppler folding is considerably small when the reflectivity factor is lower than $\sim -15$ dB$Z_{\mathrm{e}}$. This can be explained as follows. Considering the probability density function of Doppler velocity, the contribution of the area beyond $V_{\max}$ decreases. The solid and dashed lines of 7500 Hz are almost the same because $SD_{\mathrm{random}}$ itself is small and $V_{\max}$ for 7500 Hz is large (6.0 m/s).

It is difficult for the conventional unfolding method generally used by ground-based Doppler weather radar to avoid discontinuous velocity changes in order to solve the folding of isolated clouds (e.g., [41]). The ground-based measurements with W-band Super Polarimetric Ice-crystal Detection and Explication Radar (SPIDER) radar of the National Institute of Infomation and Communications Technology (NICT) [42] showed that upward motion above 3 m/s was rarely observed. In addition, the unfolding threshold used in this study was also employed in Kollias *et al.* [43] and they successfully unfolded their simulated EC-CPR Doppler velocities. Therefore, if $V_{1\,\mathrm{km},\ 10\,\mathrm{km}}$ exceeds the threshold value $V_{\mathrm{th}} = -3$ m/s (upward), then $V_{1\,\mathrm{km},\ 10\,\mathrm{km}}$ is unfolded using the following:

$$V_{\mathrm{unfolded}} = V_{1\,\mathrm{km},10\,\mathrm{km}} + 2 \cdot V_{\max}. \tag{11}$$

Although Kollias *et al.* [43] used the threshold of the reflectivity factor to judge the folding, we did not employ it, in order to correctly consider the case of the attenuated reflectivity factor.

## III. Results

Here, we examine two representative cloud system cases using the NICAM/J-Sim data. The first case is a cirrus cloud scene where the radar reflectivity factor is relatively low with a small horizontal variation of the $Z_{\mathrm{e,jsim}}$ and $V_{\mathrm{jsim}}$ fields, and Doppler folding hardly appears in $V_{\mathrm{jsim}}$. The second is a precipitation case where the radar reflectivity factor is relatively high with a large horizontal variation of the $Z_{\mathrm{e,jsim}}$ and $V_{\mathrm{jsim}}$ fields, and where folding frequently occurs in strong precipitation echoes.

### A. Cirrus Cloud Case

Fig. 3 shows the latitude-height cross sections of $Z_{\mathrm{e,jsim}}$ with $V_{\mathrm{jsim}}$ and simulated Doppler velocity ($V_{500\,\mathrm{m}}$). The gray color indicates clear sky or regions not detectable by the

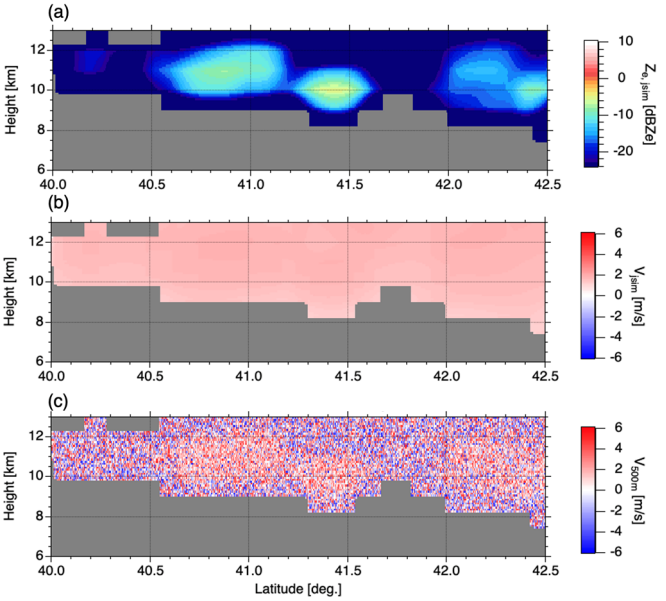


Fig. 3. Latitude-height plots of (a) NICAM/J-Sim radar reflectivity factor, (b) NICAM/J-Sim Doppler velocity, and (c) simulated Doppler velocity for 500-m integration.

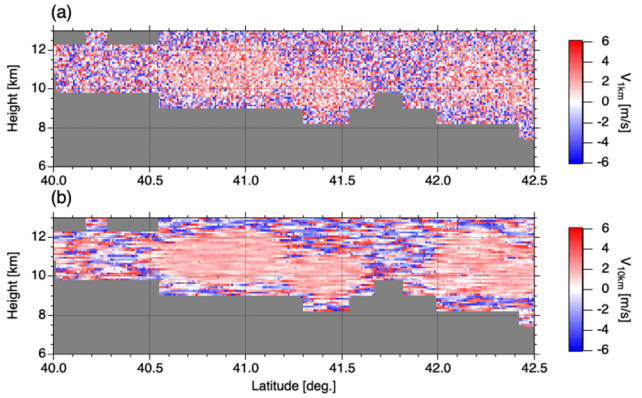


Fig. 4. Latitude-height plots of simulated Doppler velocity for (a) 1-km and (b) 10-km integration.

EC-CPR in the NICAM/J-Sim. The horizontally smooth echo signals less than $-5$ dB$Z_{\mathrm{e}}$ are located between $\sim$9 and 12 km height [Fig. 3(a)]. The $V_{\mathrm{jsim}}$ of the cirrus echo shown in Fig. 3(b) is $\sim$1.7 m/s (downward motion). Fig. 3(c) shows simulated Doppler velocity $V_{500\,\mathrm{m}}$ from $R_\tau$ using (8). Since the observation window of this area is in "high mode," the PRF of this region around 41° is about 6313 Hz (red line in Fig. 1). The $V_{\max}$ is $\sim$5.0 m/s and the number of pulse pairs ($M$) is 378. As illustrated in Fig. 2, $SD_{\mathrm{random}}$ is 1.9 m/s for $-10$ dB$Z_{\mathrm{e}}$, 2.2 m/s for $-15$ dB$Z_{\mathrm{e}}$, and 3.1 m/s for $-20$ dB$Z_{\mathrm{e}}$, respectively. Compared to $V_{\mathrm{jsim}}$ [Fig. 3(b)], the variations significantly increase and upward motion (blue dots) can be observed in $V_{500\,\mathrm{m}}$. This is because a relatively large $V_{\mathrm{random}}$ is added to $V_{\mathrm{jsim}}$, and $V_{\mathrm{m}}$ occasionally exceeds $V_{\max}$.

Fig. 4 presents the latitude-height plots of $V_{1\,\mathrm{km}}$ and $V_{10\,\mathrm{km}}$. The Random noise in $V_{500\,\mathrm{m}}$ is expected to be reduced by horizontal integration. There are still many variations of velocities in $V_{1\,\mathrm{km}}$ [Fig. 4(a)]. After the 10-km horizontal integration [Fig. 4(b)], $V_{10\,\mathrm{km}}$ with a higher reflectivity factor in Fig. 3(a)

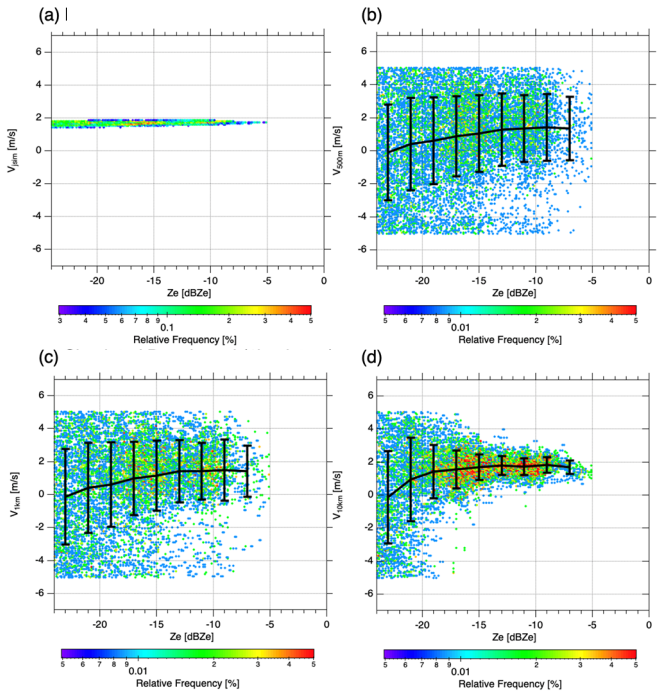


Fig. 5. 2-D histogram of (a) NICAM/J-sim, simulated for (b) 500-m integration, (c) 1-km integration, and (d) 10-km integration Doppler velocities as a function of $Z_e$. The dashed lines and error bars denote the mean and standard deviation of velocities at binned with a step of 2 dB$Z_e$.

approaches $V_{\mathrm{jsim}}$ [Fig. 3(b)]. However, a horizontally extended error is seen in $V_{10\,\mathrm{km}}$ at a lower reflectivity factor in Fig. 3(a).

To show the dependence on the reflectivity factor of the Doppler velocity change, we plot 2-D occurrence histogram of $V_{\mathrm{jsim}}$, $V_{500\,\mathrm{m}}$, $V_{1\,\mathrm{km}}$, and $V_{10\,\mathrm{km}}$ as a function of $Z_e$ in Fig. 5. The dashed lines and error bars denote the mean and standard deviation (SD) of velocities at binned with a step of 2 dB$Z_e$, respectively. In Fig. 5(a), they are omitted for the sake of readability. The mean of $V_{\mathrm{jsim}}$ is ~1.7 m/s and does not change as $Z_e$ rises [Fig. 5(a)]. The maximum SD of $V_{\mathrm{jsim}}$ is ~0.2 m/s. In contrast, the SD of $V_{500\,\mathrm{m}}$ becomes considerably large for all dB$Z_e$ (e.g., ~2.8 m/s for −23 dB$Z_e$) [Fig. 5(b)]. It can be seen also that Doppler folding occurs where the absolute values of $V_{500\,\mathrm{m}}$, $V_{1\,\mathrm{km}}$, and $V_{10\,\mathrm{km}}$ are larger than $V_{\mathrm{max}}$ (5.0 m/s). We cannot clearly see the folded negative velocities reduced by 1-km integration in Fig. 4(a). However, compared to Fig. 5(b), Fig. 5(c) shows slightly less occurrence of folded negative velocities at higher reflectivity factors. In the result of $V_{10\,\mathrm{km}}$ [Fig. 5(d)], the frequency becomes higher around the mean value of the velocity, and the SD of echo signals with values larger than −20 dB$Z_e$ is greatly reduced as compared with $V_{1\,\mathrm{km}}$ [Fig. 5(c)]. Their SD for −7 dB$Z_e$ is ~0.4 m/s.

Next, we calculated the SD from the difference between the simulated velocity (i.e., $V_{500\,\mathrm{m}}$, $V_{1\,\mathrm{km}}$, $V_{10\,\mathrm{km}}$) and $V_{\mathrm{jsim}}$(hereafter $SD_{\mathrm{diff}}$). Since the SD of $V_{\mathrm{jsim}}$ is included in the simulated velocities shown in Fig. 5(b)–(d), we evaluate $SD_{\mathrm{diff}}$ by eliminating the influence of $V_{\mathrm{jsim}}$ in Fig. 6. The dashed lines denote theoretical random errors including the folding effects corresponding to each integration length. In Fig. 6(a), the theoretical random error is reduced with the increase of $Z_e$. The $SD_{\mathrm{diff}}$ in $V_{500\,\mathrm{m}}$ also shows the same tendency. We can see

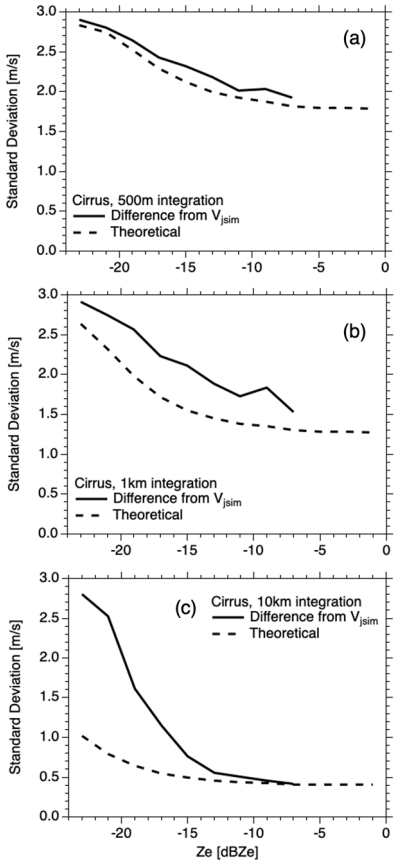


Fig. 6. Standard deviation of random error of simulated Doppler velocities as a function of radar reflectivity factor for (a) 500-m integration, (b) 1-km integration, and (c) 10-km integration. The dashed lines denote the calculated random error considering Doppler folding.

the $SD_{\mathrm{diff}}$ becomes smaller after 1-km integration with a higher reflectivity factor [Fig. 6(b)]. In the result of $V_{10\,\mathrm{km}}$ [Fig. 6(c)], The $SD_{\mathrm{diff}}$ approaches the theoretical random error as dB$Z_e$ becomes larger, suggesting that the horizontal integration very effectively reduces $SD_{\mathrm{diff}}$. For instance, the $SD_{\mathrm{diff}}$ values of $V_{500\,\mathrm{m}}$, $V_{1\,\mathrm{km}}$, and $V_{10\,\mathrm{km}}$ for −10 dB$Z_e$ are ~2.0, 1.8, and 0.5 m/s, respectively.

### *B. Precipitation Case*

Fig. 7 shows the latitude-height cross sections of $Z_{\mathrm{e,jsim}}$, $V_{\mathrm{jsim}}$, and simulated $V_{500\,\mathrm{m}}$ for the precipitation case. In Fig. 7(a), there is a melting layer around 3.5-km height, a precipitation echo below the layer, and convective clouds above the layer. In Fig. 7(b), $V_{\mathrm{jsim}}$ in the precipitation region is ~4.0 and ~2.4 m/s in the cloud region. A large spatio-temporal variation in velocities is seen compared to the cirrus case [Fig. 3(b)]. Fig. 7(c) shows the simulated Doppler velocity $V_{500\,\mathrm{m}}$ from $R_\tau$ using (8). As the observation window of this case is the high mode, the PRF of this region around 51° is about 6279 Hz as shown in Fig. 1. The $V_{\mathrm{max}}$ is ~5.0 m/s and the number of pulse pairs ($M$) is 378. For example, $SD_{\mathrm{random}}$ is 1.8 m/s for 0 dB$Z_e$, 1.9 m/s for −10 dB$Z_e$, and 3.1 for −20 dB$Z_e$ (Fig. 2). As compared with $V_{\mathrm{jsim}}$ [Fig. 7(b)], the striking increase in the variations of velocities and upward motion (blue dots) becomes noticeable

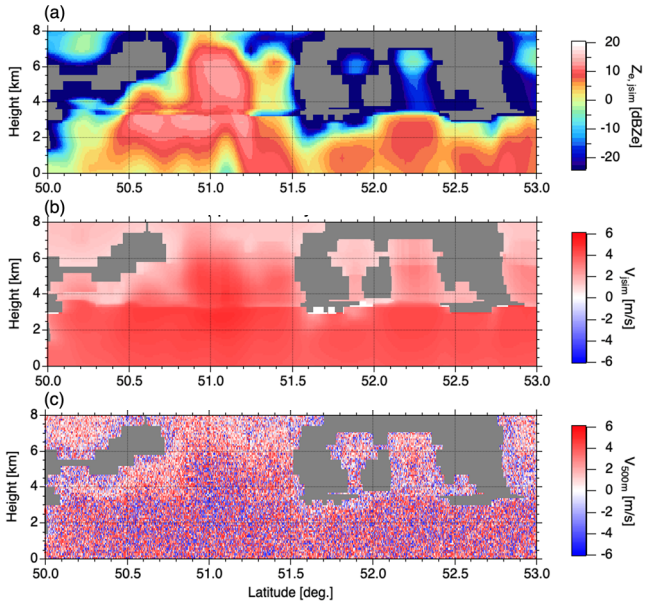


Fig. 7. Latitude-height plots of (a) NICAM/J-Sim radar reflectivity factor, (b) NICAM/J-Sim Doppler velocity, and (c) simulated Doppler velocity for 500-m integration.

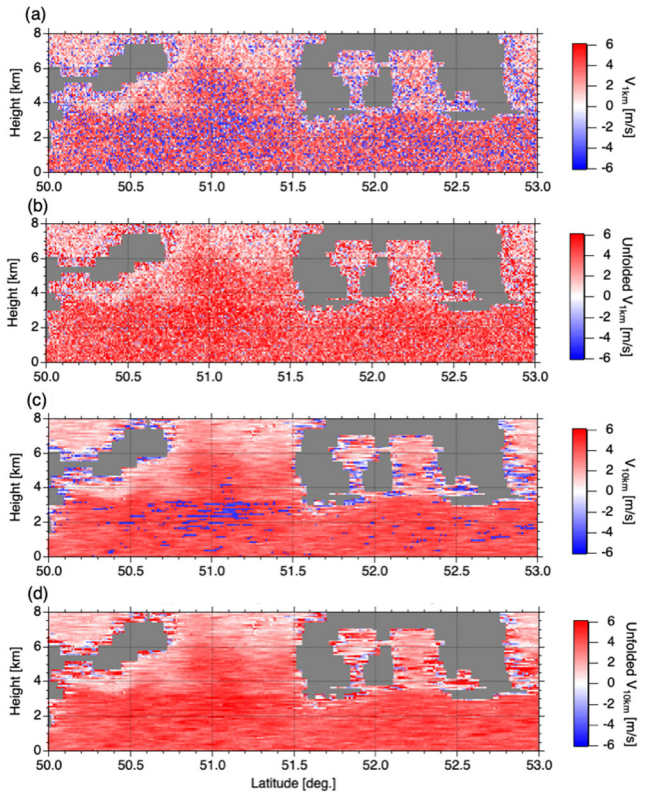


Fig. 8. Latitude-height plots of the simulated Doppler velocity for (a) 1-km integration, (b) unfolded 1-km integration, (c) 10-km integration, and (d) unfolded 10-km integration.

in $V_{500\,\mathrm{m}}$. This is because a relatively large $V_{\mathrm{random}}$ is added to $V_{\mathrm{jsim}}$. Additionally, $V_{\mathrm{m}}$ frequently exceeds $V_{\mathrm{max}}$ in the precipitation region due to the large $V_{\mathrm{jsim}}$.

Fig. 8 illustrates the latitude-height plots of $V_{1\,\mathrm{km}}$, unfolded $V_{1\,\mathrm{km}}$, $V_{10\,\mathrm{km}}$, and unfolded $V_{10\,\mathrm{km}}$. After 1-km integration, large

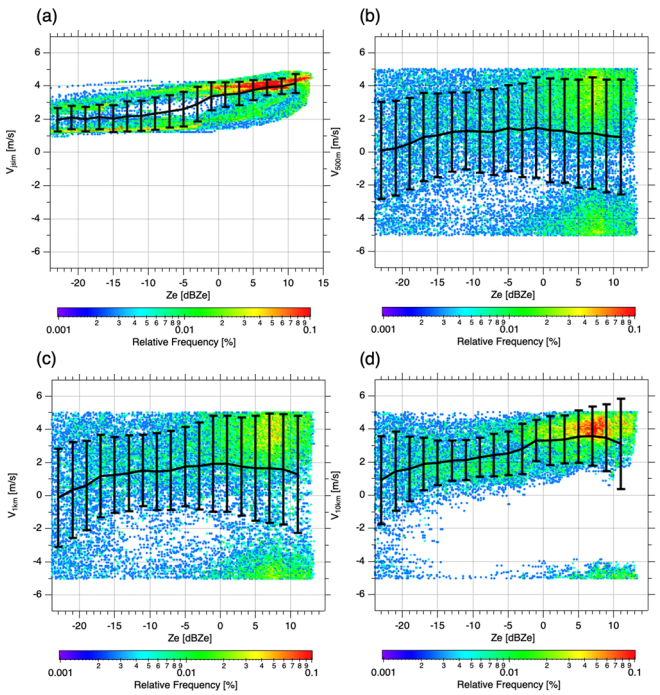


Fig. 9. 2-D histogram of (a) NICAM/J-sim, simulated for (b) 500-m integration, (c) 1-km integration, and (d) 10-km integration Doppler velocities as a function of $Z_{\mathrm{e}}$. The dashed lines and error bars denote the mean and standard deviation of velocities at binned with a step of 2 dB$Z$.

variations in velocities and upward motion (blue dots) are still present in $V_{1\,\mathrm{km}}$ [Fig. 8(a)]. In addition to the horizontal integration, by applying velocity unfolding using (11), the upward motion almost disappears in the unfolded $V_{1\,\mathrm{km}}$ [Fig. 8(b)]. In Fig. 8(c), variations in velocities are reduced but some negative values remain in areas with large $Z_{\mathrm{e}}$ and near the cloud edges. In Fig. 8(d), the unfolded $V_{10\,\mathrm{km}}$ after unfolding approaches $V_{\mathrm{jsim}}$ [Fig. 7(b)].

We examined the dependence on reflectivity factors of the variances of Doppler velocity. Fig. 9 depicts a 2-D histogram of $V_{\mathrm{jsim}}$, $V_{500\,\mathrm{m}}$, $V_{1\,\mathrm{km}}$, and $V_{10\,\mathrm{km}}$ as a function of the $Z_{\mathrm{e}}$. The dashed lines and error bars denote the mean and SD of velocities, respectively, binned with a step of 2 dB$Z_{\mathrm{e}}$. In Fig. 9(a), the mean of $V_{\mathrm{jsim}}$ increases as $Z_{\mathrm{e}}$ rises and reaches 3 to 4 m/s for $Z_{\mathrm{e}}$ above 0 dB$Z_{\mathrm{e}}$, the frequency is correspondingly high. The SD is $\sim$1.0 m/s for $-5$ dB$Z_{\mathrm{e}}$ and $\sim$0.6 m/s for 5 dB$Z_{\mathrm{e}}$. Although the SD of $V_{500\,\mathrm{m}}$ for $Z_{\mathrm{e}}$ below $-11$ dB$Z_{\mathrm{e}}$ is reduced to $\sim$2.3 m/s, those for $Z_{\mathrm{e}}$ above $-11$ dB$Z_{\mathrm{e}}$ increases up to $\sim$3.5 m/s [Fig. 9(b)]. This is attributed to many folded negative values at larger $Z_{\mathrm{e}}$ due to the large $V_{\mathrm{jsim}}$. This can be clearly seen from the two high-frequency areas in Fig. 5(b). That is, the portion of one of the more frequent positive velocities that exceed $V_{\mathrm{max}}$ is folded and appears in negative. This feature is not seen in $V_{500\,\mathrm{m}}$ of the cirrus cloud case in Fig. 5(b) because the velocities in the cirrus case are smaller. The tendency in $V_{500\,\mathrm{m}}$ [Fig. 9(b)] is also found in $V_{1\,\mathrm{km}}$ [Fig. 9(c)]. As seen in Fig. 9(d), the SD is significantly decreased by 10-km integration (e.g., $\sim$1.2 m/s for $-11$ dB$Z_{\mathrm{e}}$). This is well illustrated by the fact that the high-frequency areas, such as those seen in Fig. 9(b) and (c), were mainly only found for positive velocities. However, some

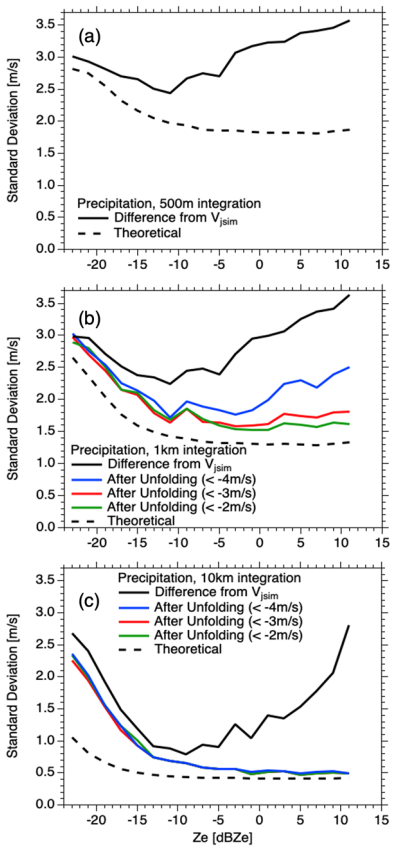


Fig. 10. Standard deviation of random error of simulated Doppler velocities as a function of radar reflectivity factor for (a) 500-m integration, (b) 1-km integration, and (c) 10-km integration. The unfolding results are shown for different thresholds: –4 m/s (blue), –3 m/s (red), and –2 m/s (green). The dashed lines denote theoretical random error considering Doppler folding.

negative values are still found at larger $Z_e$, corresponding to the blue dots shown in areas with large $Z_e$ and near the cloud edges [Fig. 8(c)].

Fig. 10 shows the $SD_{diff}$ of $V_{500\,m}$, $V_{1\,km}$, $V_{10\,km}$ as a function of $Z_e$. The unfolded results using (11) are also illustrated in Fig. 10. The dashed lines denote theoretical random errors considering velocity folding. In Fig. 10(a), the $SD_{diff}$ of $V_{500\,m}$ decreases for $Z_e$ below to $-11$ dB$Z_e$ and increases for $Z_e$ above $-11$ dB$Z_e$. The decrease of $SD_{diff}$ stems from the reduction of random error, whereas the increase of $SD_{diff}$ is caused by the occurrence of velocity folding due to the large $V_{jsim}$ as shown in Fig. 9(a). After 1-km integration [Fig. 10(b)], the $SD_{diff}$ of $V_{1\,km}$ is smaller than that of $V_{500\,m}$ and the same tendency is seen for $Z_e$ dependence. When the unfolding method is applied, the $SD_{diff}$ of $V_{1\,km}$ decreases considerably as the folded negative velocities are corrected and its appearance is reduced. If we change the threshold of unfolding method $V_{th}$, the $SD_{diff}$ of $V_{1\,km}$ with $V_{th} = -4$ m/s is rather large and increases at larger $Z_e$. Meanwhile, the $SD_{diff}$ of $V_{1\,km}$ with $V_{th} = -2$ and$-3$ m/s becomes close to theoretical random error and does not increase at large $Z_e$. In Fig. 10(c), the $SD_{diff}$ of $V_{10\,km}$ drops substantially compared to the $SD_{diff}$ of $V_{1\,km}$ and reaches 0.8 m/s at $-9$ dB$Z_e$. It increases for $Z_e$ above $-9$ dB$Z_e$ as $Z_e$ becomes larger. If the unfolding method is applied, the $SD_{diff}$ of $V_{10\,km}$ is reduced and it significantly decreases above $-9$ dB$Z_e$. For example, the $SD_{diff}$ of $V_{10\,km}$ is $\sim$0.9 m/s at $-15$ dB$Z_e$, and less than 0.5 m/s above 0 dB$Z_e$, respectively. Regarding $SD_{diff}$ of $V_{10\,km}$, there is no significant difference between the results of $V_{th} = -2$, $-3$, and$-4$ m/s. This is attributed to the fact that very few echoes exist between $-4$ and$-2$ m/s in Fig. 9(d). Compared to the cirrus cloud case, in addition to the horizontal integration, the correction of velocity folding successfully reduces $SD_{diff}$.

We note that random error reduction was performed by others using optimized low-pass filters in the along-track direction in Fourier spectrum space [44]. The method was applied to the simulated marine stratiform clouds case [45]. We understand that it reduces the root-mean-square (rms) error while preserving the spatial features of the Doppler field. However, 1- and 10-km horizontal integrated Doppler products are required for the JAXA standard algorithms. We have examined the rms differences between original $V_{jsim}$ and 10-km integrated $V_{jsim}$. The differences are 0.12 for the cirrus case and 0.17 m/s for the precipitation case.

## IV. Conclusion

We examined EarthCARE CPR (EC-CPR) Doppler velocity measurement errors introduced by Doppler broadening and folding, in order to evaluate and improve Doppler data processing in the JAXA standard algorithm. We used globally simulated EC-CPR observation data (NICAM/J-Sim $Z_{e,jsim}$ and $V_{jsim}$) with the same footprint and vertical resolution simulated by a GCSRM and a satellite data simulator. The EC-CPR-observed Doppler velocities were calculated for 500-m, 1-km, and 10-km horizontal integration using horizontally integrated pulse-pair covariances with the latest EC-CPR specifications. Their Doppler-folding-corrected velocities were also calculated using our unfolding method. We evaluated the standard deviation of random errors ($SD_{diff}$) to investigate the effectiveness of horizontal integration and the unfolding method for the reduction of errors.

Two representative cases of cirrus clouds and precipitation were examined. In the cirrus cloud case, the radar reflectivity factor was relatively low, with small horizontal variations of the $Z_{e,jsim}$ and $V_{jsim}$ fields, and Doppler folding did not appear in $V_{jsim}$. The $SD_{diff}$ decreased when the integration length became large. The values of $SD_{diff}$ for $-10$ dB$Z_e$ cloud echoes were about 2.0 for 500-m integration, 1.8 for 1-km integration, and 0.5 m/s for 10-km integration, respectively. Note that, as $Z_e$ became larger, the result of 10-km integration approached theoretical random error including the Doppler folding effect.

In the precipitation case, the radar reflectivity factor was relatively high, with large horizontal variations of the $Z_{e,jsim}$ and $V_{jsim}$ fields, and folding frequently occurred in $V_{jsim}$. The values of $SD_{diff}$ for 500-m integration decreased for $Z_e$ below $-11$ dB$Z_e$ as in the cirrus cloud case, but $SD_{diff}$ increased for $Z_e$ above $-11$ dB$Z_e$ due to the frequent occurrence of velocity folding (i.e., falling velocity of raindrops approached the folding velocity at larger $Z_e$). A similar tendency was seen in cases of 1- and 10-km integration. The unfolding method was thus needed to estimate the true

velocity. Finally, the unfolded $SD_{\text{diff}}$ for 10-km integration achieved 0.9 m/s for $-15$ dB$Z_{\text{e}}$ and less than 0.5 m/s above 0 dB$Z_{\text{e}}$, and approached the theoretical random error.

In summary, we introduced the methodology to investigate possible observation errors of a rather challenging sensor (spaceborne Doppler CPR) using GCSRM output and a satellite data simulator. We found that $SD_{\text{diff}}$ was expected to be less than 1.0 m/s above $-15$ dB$Z_{\text{e}}$ by applying 10-km horizontal integration and the unfolding method. In this study, the PRF is based high mode on a PRF setting of the EC-CPR, and thus we expect that $SD_{\text{diff}}$ could be improved by setting the low-mode PRF. This study will also contribute to the development of a satellite data simulator that can simulate realistic Doppler velocities of the EC-CPR by using input data at a finer resolution (at a subfootprint resolution, with EC-CPR's footprint of $\sim$800 m).

Two cases were analyzed in this article. A large number of case studies is needed for a more general evaluation of our current Doppler data processing, thereby leading to improvement of the JAXA standard algorithm. Although a large length of horizontal integration can reduce random error, at the same time it washes out the small scale characteristics of the radar reflectivity factor and Doppler velocity within the integrated length. The distribution of clouds in the EC-CPR footprint also affects the accuracy of Doppler velocity relative to the NUBF. In the future, we will investigate the uncertainty of Doppler velocities from heterogeneous clouds in the EC-CPR footprint with higher spatial resolution cloud fields derived from large eddy simulation or airborne data.

## ACKNOWLEDGMENT

The authors are grateful to members of the JAXA EarthCARE Science Team. The authors would like to thank Prof. Hajime Okamoto of Kyusyu University, and Prof. Anthony Illingworth of University of Reading.

## REFERENCES

[1] A. J. Illingworth *et al.*, "The EarthCARE satellite: The next step forward in global measurements of clouds, aerosols, precipitation, and radiation," *Bull. Amer. Meteorol. Soc.*, vol. 96, no. 8, pp. 1311–1332, 2015.

[2] G. L. Stephens *et al.*, "CloudSat mission: Performance and early science after the first year of operation," *J. Geophys. Res.*, vol. 113, no. 8, pp. 1–18, Dec. 2008.

[3] D. M. Winker *et al.*, "Overview of the CALIPSO mission and CALIOP data processing algorithms," *J. Atmos. Ocean. Technol.*, vol. 26, no. 11, pp. 2310–2323, Nov. 2009.

[4] G. Stephens *et al.*, "CloudSat and CALIPSO within the A-train: Ten years of actively observing the Earth system," *Bull. Amer. Meteorol. Soc.*, vol. 99, no. 3, pp. 569–581, Mar. 2018.

[5] Y. Hagihara, H. Okamoto, and R. Yoshida, "Development of a combined CloudSat-CALIPSO cloud mask to show global cloud distribution," *J. Geophys. Res.*, vol. 115, no. 17, Sep. 2010, Art. no. D00H33.

[6] R. Yoshida, H. Okamoto, Y. Hagihara, and H. Ishimoto, "Global analysis of cloud phase and ice crystal orientation from cloud-aerosol lidar and infrared pathfinder satellite observation (CALIPSO) data using attenuated backscattering and depolarization ratio," *J. Geophys. Res.*, vol. 115, no. 16, Aug. 2010, Art. no. D00H32.

[7] M. Kikuchi *et al.*, "Development of algorithm for discriminating hydrometeor particle types with a synergistic use of CloudSat and CALIPSO," *J. Geophys. Res., Atmos.*, vol. 122, no. 20, pp. 11022–11044, 2017.

[8] A. J. Heymsfield *et al.*, "Testing IWC retrieval methods using radar and ancillary measurements with *in situ* data," *J. Appl. Meteorol. Climatol.*, vol. 47, no. 1, pp. 135–163, Jan. 2008.

[9] K. Sato, H. Okamoto, T. Takemura, H. Kumagai, and N. Sugimoto, "Characterization of ice cloud properties obtained by shipborne radar/lidar over the tropical western pacific ocean for evaluation of an atmospheric general circulation model," *J. Geophys. Res.*, vol. 115, no. D15, pp. 1–18, 2010.

[10] Z. J. Luo, G. Y. Liu, and G. L. Stephens, "Use of A-train data to estimate convective buoyancy and entrainment rate," *Geophys. Res. Lett.*, vol. 37, no. 9, pp. 1–5, 2010.

[11] Y. Hagihara, H. Okamoto, and Z. J. Luo, "Joint analysis of cloud top heights from CloudSat and CALIPSO: New insights into cloud top microphysics," *J. Geophys. Res., Atmos.*, vol. 119, no. 7, pp. 4087–4106, 2014.

[12] D. Rosenfeld, S. Sherwood, R. Wood, and L. Donner, "Climate effects of aerosol-cloud interactions," *Science*, vol. 343, no. 6169, pp. 379–380, Jan. 2014.

[13] M. Satoh *et al.*, "Global cloud-resolving models," *Current Climate Change Rep.*, vol. 5, no. 3, pp. 172–184, Sep. 2019.

[14] B. Stevens *et al.*, "DYAMOND: The DYnamics of the atmospheric general circulation modeled on non-hydrostatic domains," *Prog. Earth Planet. Sci.*, vol. 6, no. 1, p. 61, Dec. 2019.

[15] H. Masunaga *et al.*, "Satellite data simulator unit: A multisensor, multispectral satellite simulator package," *Bull. Amer. Meteorol. Soc.*, vol. 91, no. 12, pp. 1625–1632, 2010.

[16] T. Hashino *et al.*, "Evaluating cloud microphysics from NICAM against CloudSat and CALIPSO," *J. Geophys. Res., Atmos.*, vol. 118, no. 13, pp. 7273–7292, Jul. 2013.

[17] T. Inoue, M. Satoh, Y. Hagihara, H. Miura, and J. Schmetz, "Comparison of high-level clouds represented in a global cloud system–resolving model with CALIPSO/CloudSat and geostationary satellite observations," *J. Geophys. Res.*, vol. 115, no. 10, 2010, Art. no. D00H22.

[18] M. Satoh, T. Inoue, and H. Miura, "Evaluations of cloud properties of global and local cloud system resolving models using CALIPSO and CloudSat simulators," *J. Geophys. Res.*, vol. 115, no. 4, Feb. 2010, Art. no. D00H14.

[19] S. Kotsuki, K. Terasaki, and T. Miyoshi, "GPM/DPR precipitation compared with a 3.5-km-resolution NICAM simulation," *SOLA*, vol. 10, no. 1, pp. 204–209, 2014.

[20] W. Roh and M. Satoh, "Extension of a multisensor satellite radiance-based evaluation for cloud system resolving models," *J. Meteorol. Soc. Jpn. II*, vol. 96, no. 1, pp. 55–63, 2018.

[21] W. Roh, M. Satoh, and T. Nasuno, "Improvement of a cloud microphysics scheme for a global nonhydrostatic model using TRMM and a satellite simulator," *J. Atmos. Sci.*, vol. 74, no. 1, pp. 167–184, Jan. 2017.

[22] T. Hashino *et al.*, "Evaluating arctic cloud radiative effects simulated by NICAM with A-train: Evaluating cloud radiative effects," *J. Geophys. Res., Atmos.*, vol. 121, no. 12, pp. 7041–7063, Jun. 2016.

[23] S. Kobayashi, H. Kumagai, and H. Kuroiwa, "A proposal of pulse-pair Doppler operation on a spaceborne cloud-profiling radar in the W band," *J. Atmos. Ocean. Technol.*, vol. 19, no. 9, pp. 1294–1306, Sep. 2002.

[24] A. Battaglia and P. Kollias, "Using ice clouds for mitigating the EarthCARE Doppler radar mispointing," *IEEE Trans. Geosci. Remote Sens.*, vol. 53, no. 4, pp. 2079–2085, Apr. 2015.

[25] S. Tanelli, E. Im, S. L. Durden, L. Facheris, and D. Giuli, "The effects of nonuniform beam filling on vertical rainfall velocity measurements with a spaceborne Doppler radar," *J. Atmos. Ocean. Technol.*, vol. 19, no. 7, pp. 1019–1034, 2002.

[26] N. A. J. Schutgens, "Simulated Doppler radar observations of inhomogeneous clouds: Application to the EarthCARE space mission," *J. Atmos. Ocean. Technol.*, vol. 25, no. 1, pp. 26–42, Jan. 2008.

[27] H. Tomita and M. Satoh, "A new dynamical framework of nonhydrostatic global model using the icosahedral grid," *Fluid Dyn. Res.*, vol. 34, no. 6, pp. 357–400, Jun. 2004.

[28] M. Satoh, T. Matsuno, H. Tomita, H. Miura, T. Nasuno, and S. Iga, "Nonhydrostatic icosahedral atmospheric model (NICAM) for global cloud resolving simulations," *J. Comput. Phys.*, vol. 227, no. 7, pp. 3486–3514, Mar. 2008.

[29] M. Satoh *et al.*, "The non-hydrostatic icosahedral atmospheric model: Description and development," *Prog. Earth Planet. Sci.*, vol. 1, no. 18, pp. 1–32, Dec. 2014.

[30] D. E. Waliser *et al.*, "The 'year' of tropical convection (May 2008–April 2010): Climate variability and weather highlights," *Bull. Amer. Meteorol. Soc.*, vol. 93, no. 8, pp. 1189–1218, 2012.

[31] M. Satoh, W. Roh, and T. Hashino, "Evaluations of clouds and precipitations in NICAM using the joint simulator for satellite sensors," CGER's Supercomput. Monogr., Tech. Rep. CGER-I127-2016, 2016, p. 110, vol. 22. [Online]. Available: http://www.cger.nies.go.jp/publications/report/i127/en/

[32] H. Okamoto, "An algorithm for retrieval of cloud microphysics using 95-GHz cloud radar and lidar," *J. Geophys. Res.*, vol. 108, no. D7, pp. 1–21, 2003.

[33] H. Okamoto *et al.*, "Vertical cloud structure observed from shipborne radar and lidar: Midlatitude case study during the MR01/K02 cruise of the research vessel Mirai," *J. Geophys. Res.*, vol. 112, no. D8, pp. 1–22, 2007.

[34] H. Okamoto *et al.*, "Vertical cloud properties in the tropical western Pacific ocean: Validation of the CCSR/NIES/FRCGC GCM by shipborne radar and lidar," *J. Geophys. Res.*, vol. 113, no. D24, pp. 1–17, 2008.

[35] T. Nishizawa, H. Okamoto, T. Takemura, N. Sugimoto, I. Matsui, and A. Shimizu, "Aerosol retrieval from two-wavelength backscatter and one-wavelength polarization lidar measurement taken during the MR01K02 cruise of the R/V *Mirai* and evaluation of a global aerosol transport model," *J. Geophys. Res., Atmos.*, vol. 113, no. 21, pp. 1–18, 2008.

[36] R. J. Doviak and D. S. Zrnic, *Doppler Radar and Weather Observations*. New York, NY, USA: Academic, 1993.

[37] S. Kobayashi, H. Kumagai, and T. Iguchi, "Accuracy evaluation of Doppler velocity on a spaceborne weather radar through a random signal simulation," *J. Atmos. Ocean. Technol.*, vol. 20, no. 6, pp. 944–949, Jun. 2003.

[38] E. E. Gossard *et al.*, "The potential of 8-mm radars for remotely sensing cloud drop size distributions," *J. Atmos. Ocean. Technol.*, vol. 14, no. 1, pp. 76–87, Feb. 1997.

[39] P. Amayenc, J. Testud, and M. Marzoug, "Proposal for a spaceborne dual-beam rain radar with Doppler capability," *J. Atmos. Ocean. Technol.*, vol. 10, no. 3, pp. 262–276, Jun. 1993.

[40] A. Battaglia, S. Tanelli, and P. Kollias, "Polarization diversity for millimeter spaceborne Doppler radars: An answer for observing deep convection?" *J. Atmos. Ocean. Technol.*, vol. 30, no. 12, pp. 2768–2787, Dec. 2013.

[41] P. S. Ray and C. Ziegler, "De-aliasing first-moment Doppler estimates," *J. Appl. Meteorol.*, vol. 16, no. 5, pp. 563–564, May 1977.

[42] H. Horie, T. Iguchi, H. Hanado, H. Kuroiwa, H. Okamoto, and H. Kumagai, "Development of a 95-GHz airborne cloud profiling radar (SPIDER)–Technical aspects," *IEICE Trans. Commun.*, vol. 83, no. 9, pp. 2010–2020, 2000.

[43] P. Kollias, S. Tanelli, A. Battaglia, and A. Tatarevic, "Evaluation of EarthCARE cloud profiling radar Doppler velocity measurements in particle sedimentation regimes," *J. Atmos. Ocean. Technol.*, vol. 31, no. 2, pp. 366–386, Feb. 2014.

[44] O. O. Sy, S. Tanelli, P. Kollias, and Y. Ohno, "Application of matched statistical filters for EarthCARE cloud Doppler products," *IEEE Trans. Geosci. Remote Sens.*, vol. 52, no. 11, pp. 7297–7316, Nov. 2014.

[45] D. Burns, P. Kollias, A. Tatarevic, A. Battaglia, and S. Tanelli, "The performance of the EarthCARE cloud profiling radar in marine stratiform clouds," *J. Geophys. Res., Atmos.*, vol. 121, no. 24, pp. 14525–14537, Dec. 2016.